

# DSGN++: Exploiting Visual-Spatial Relation for Stereo-based 3D Detectors

Yilun Chen, *Student Member, IEEE*, Shijia Huang, *Student Member, IEEE*,  
Shu Liu, *Member, IEEE*, Bei Yu, *Member, IEEE*, Jiaya Jia, *Fellow, IEEE*

**Abstract**—Camera-based 3D object detectors are welcome due to their wider deployment and lower price than LiDAR sensors. We revisit the prior stereo modeling DSGN about the stereo volume constructions for representing both 3D geometry and semantics. We polish the stereo modeling and propose our approach, DSGN++, aiming for improving information flow throughout the 2D-to-3D pipeline in the following three main aspects. First, to effectively lift the 2D information to stereo volume, we propose depth-wise plane sweeping (DPS) that allows denser connections and extracts depth-guided features. Second, for better grasping differently spaced features, we present a novel stereo volume – Dual-view Stereo Volume (DSV) that integrates front-view and top-view features and reconstructs sub-voxel depth in the camera frustum. Third, as the foreground region becomes less dominant in 3D space, we firstly propose a multi-modal data editing strategy – Stereo-LiDAR Copy-Paste, which ensures cross-modal alignment and improves data efficiency. Without bells and whistles, extensive experiments in various modality setups on the popular KITTI benchmark show that our method consistently outperforms other camera-based 3D detectors for all categories. Code will be released at <https://github.com/chenyilun95/DSGN2>.

**Index Terms**—3D Object Detection, Stereo Matching, Autonomous Driving.

## 1 INTRODUCTION

CAMERA-based 3D visual perception is a fundamental and challenging task in 3D computer vision, which serves as the essential component for autonomous driving and robotics.

The main difficulty of camera-based 3D detectors lies in the fact that *cameras provide front-view information but generally lack top-view cues or depth for accurate 3D object localization*. A common choice for camera-based 3D detectors is to leverage the successful 2D object detectors [1], [2], [3], [4] and depth estimators [5], [6], [7]. A series of approaches [8], [9], [10], [11], [12], [13], [14], [15], [16] design complicated strategies to predict 3D boxes under the constraint of projective geometry.

Differently, the 2D-to-3D transformation converts the problem to 3D modeling, which avoids the dimensionality loss in solving 3D problems. In particular, the problem of 3D detection can be solved innately by predicting objects over every 3D spatial location. For instance, Pseudo-LiDARs [17], [18], [19] generate explicit 3D representation followed by direct application of 3D detectors [20], [21], [22]. The explicit 3D form via, *e.g.*, depth maps, occupancy grids, or pseudo point clouds, removes the uncertainty and decouples the tasks of depth estimation and object recognition.

However, depth prediction is an ill-posed issue and cost volume reflects the uncertainty of voxel occupancy state. To preserve the knowledge of depth uncertainty, the modeling of geometry-guided volume becomes popular in

recent approaches [23], [24], [25], [26], [27]. 3D geometry (or epipolar geometry) is encoded into the concrete 3D voxel grids and guides the following 3D prediction. In essence, feature transformation from 2D to 3D representation avoids the loss of geometric uncertainty, which is proved influential for following 3D prediction [23].

Therefore, valid information lifting (also gradient flow) from 2D semantics to stereo volume controls the effectiveness of 2D-to-3D modeling and determines the following 3D prediction quality. However, current 3D modeling remains as an approximation of realistic 3D representation and thus poses three critical challenges for building effective stereo volumes in 3D space as follows:

(I) *Direct 2D-to-3D information lifting constrains volumetric representation learning*. In geometric modeling, *plane sweeping* (PS) [28], [29], [30] is the dominant way to lift 2D information to 3D volume. Specifically, per-view features are directly propagated by tracing the ray in the volumetric space [6], [7] for matching the pixel differences. As 3D volume computation cost is one more order of magnitude higher than 2D network, per-view features are commonly compressed to reduce calculation costs. As a consequence, the stereo representation is constrained by the small number of feature channels. Our findings indicate that relieving this bottleneck unleashes the power of volumetric representation for complicated prediction tasks.

(II) *Perception of differently shaped objects*. By plane sweeping, we can produce two views of stereo volumes: Plane-sweep volume (PSV) in camera frustum and 3D-geometry volume (3DGV) in regular 3D space. However, real-world 3D objects are non-rigid and irregular-shaped. Some categories like *Pedestrian* occupy fewer voxel occupancies in the bird’s eye view albeit being clearly visible in the front view. In our study, these single-view stereo volumes show

- Y. Chen, S. Huang, B. Yu and J. Jia are with the Department of Computer Science and Engineering, The Chinese University of Hong Kong, Hong Kong, China.  
E-mail: {y1chen, sjhuang, byu, leojia}@cse.cuhk.edu.hk; liushuhust@gmail.com
- J. Jia and S. Liu are with the SmartMore.

varied properties. Plane-sweep volume tends to extract better features for front-view objects (such as *Pedestrian* and *Cyclist*) while 3D-geometry volume gets the same gradient value for the same object at different distances.

(III) *Biased modeling*. The proportion of the foreground region is normally small in the aerial view for outdoor scenes, which raises the difficulty in generating unbiased estimation of each location towards foreground/background. Besides, imbalanced class distribution also gives the biased gradient flow towards different categories and suppresses the generalization ability of stereo modeling.

In this paper, we provide the following three solutions for addressing the above challenges in the 2D-to-3D modeling. By polishing the overall stereo modeling, we present a simple yet effective stereo-based 3D detection framework DSGN++.

First, we present a generic operator for 2D-to-3D transformation – *depth-wise plane sweeping* (D-PS) to relieve the bottleneck of 2D-to-3D information propagation. With D-PS, the transformation allows the input of wider 2D features, that encodes depth-guided features within its expanded channels. And the generated volume yields *continuously changing* features that slice the 2D features via the sliding window technique. A key component called “cyclic slicing” is employed to realize *local feature continuity* for nearby depth planes. Experiments demonstrate its notable improvement for both monocular and binocular camera-based 3D object detection.

Second, we provide a new form of stereo volumetric representation – Dual-view Stereo Volume (DSV) to build more extensive connections to different views. In particular, we aggregate features of differently-shaped voxels from the front view (plane-sweep volume) and top view (3D-geometry volume). The final cost volume is produced by a front-surface depth head including a front-view 3D transformation where the geometric supervision of sub-voxel depth values provides better supervision signals than discretized voxel occupancy learning.

Last, to overcome the limited foreground regions in 3D modeling and make unbiased predictions towards categories, we seek to apply the copy-paste strategy [31]. However, the requirement of precise cross-modal alignment restricts the freedom of data editing. To overcome the limitation, we propose *Stereo-LiDAR Copy-Paste* (SLCP) that allows joint stereo and 3D data editing and meets the constraint of cross-modal projection. We validate this flexible data editing improves modeling efficiency and generalization ability to various categories.

Our total contribution is fourfold.

- Without additional computation, we propose a novel volume construction approach of *depth-wise plane sweeping* (D-PS) to expand the information flow capacity and extract depth-relevant 2D features.
- We propose Dual-view Stereo Volume that aggregates the information flow from two different 3D volumes and investigates its effectiveness over prior constructions.
- For the first time, the method augments multi-modal data pair by *Stereo-LiDAR Copy-Paste* strategy that ensures the stereo alignments at the sub-pixel level and improves

the data efficiency. We prove that the strategy greatly mitigates the class imbalanced problem.

- Without bells and whistles, our proposed DSGN++ achieves the **first** place for **all categories** among all camera-based approaches on the challenging KITTI benchmark [32] on Nov 20, 2021, and even surpasses some LiDAR detectors in  $AP_{3D}$ , such as AVOD [33] for the first time.

## 2 RELATED WORK

**Stereo Matching and Multi-View Stereo.** In the field of stereo matching, methods of [6], [7], [34], [35], [36], [37] process the left and right images by a Siamese network and construct a 3D cost volume to compute the matching cost. Correlation-based cost volume is applied in recent work [35], [38], [39], [40], [41], [42]. Methods of [6], [7] form a concatenation-based cost volume and apply 3D convolution to regress disparity estimates. For multi-view scene reconstruction, prior work [30], [43], [43], [44], [45], [46], [47], [48] even achieves fewer depth errors than RGB-D sensors, which shows great potential to be an alternative of expensive depth sensors. MVSMachine [43] proposes the differentiable projection and unprojection for better extracting 3D to manipulate the volume construction from multi-view images.

**LiDAR-based 3D Detection.** LiDAR sensors are very powerful to produce data for 3D detectors. The target of LiDAR-based detectors is to extract discriminative features from point clouds for 3D object recognition. There are generally two types of 3D representations, i.e., voxel-based representation [22], [49], [50], [51] and point-based representation [20], [52], [53], [54], [55]. Albeit depth sensors (*e.g.*, LiDAR sensors and RGB-D cameras) can retrieve accurate depth cues, they are generally more expensive and are with sparser sensing resolution than the common off-the-shelf RGB cameras. We prove that with a simple fusion strategy, our stereo modeling can further promote the performance of LiDAR-based 3D detectors.

**Camera-based 3D Detection.** In contrast to the high cost and sparse resolution of depth sensors, cameras are readily available and applied on a wide scale. The dense imaging resolutions ( $> 720P$ ) provide human-readable semantics that is easy to distinguish. The accessibility and dominance as the basic perception sensor in the real world make it attractive to perceive and understand 3D scenes. We classify methods into two types according to their intermediate 2D or 3D representation. The key difference is that 2D representation extracts features in the front view while 3D or bird’s eye view (BEV) type extracts features in top views or 3D space.

For 2D representation-based 3D detector, an intuitive solution is to leverage a 2D object detector [3], [4]. Similar to 2D object detectors, prior work [8], [9], [11], [14], [15], [16], [56], [57], [58], [59] directly estimates 3D bounding boxes from camera images and relies on perspective modeling of the 2D projected object and its 3D objects. On the other hand, depth supervision via point clouds or depth maps is accessible during training. Explicit learning of depth cues improves the accuracy of 3D object detection [60]. Methods

of [10], [12], [61] also jointly aggregate the learned depth cues and semantic cues.

Generally, due to the consistency with 3D spaces, the 3D form provides an elegant and effective representation with no complicated post-processing steps. 3DOP [62], [63] generates point cloud by stereo and encodes the prior knowledge and depth in an energy function. Several methods [17], [18], [19] transform the depth map to Pseudo-LiDAR with point cloud followed by another independent network. Pseudo-LiDAR [17], [18], [19], [64] introduces the pseudo point clouds as the intermediate 3D representation followed by a LiDAR-based 3D detector. This pipeline yields much improvement over previous 2D representation-based approaches. E2E-PL [25] further enables back-propagation to depth coordinates by introducing radial basis functions. We note that these methods are limited to explicit modeling of depth maps. They compress the abundant information from pixel-level feature projection and correspondence.

Other methods of [23], [24], [26], [65], [66], [67] utilize 3D feature volumes to enable end-to-end training. Recently DSGN [23] performs remarkably by implicitly encoding 3D geometry into neural networks. CDN [67] further refine depth prediction near object boundaries via a Wasserstein distance-based loss. PLUME [24] designs the efficient 3D-BEV network to achieve proper trade-off between speed and accuracy. LIGA-stereo [27] further leverages the well-learned LiDAR-detector to transfer the knowledge to DSGN and demonstrates the effectiveness of cross-modal distillation [68].

### 3 OUR APPROACH

In Sec. 3.1, as a prerequisite, we revisit the stereo volume transformation in DSGN [23] that encodes the implicit geometric and semantic cues. We then introduce our DSGN++ model (shown in Fig. 1) to significantly improve the capacity of stereo modeling in the following three aspects.

First, we identify the network bottleneck that limits the quantity of information flow and introduce a generic operator – depth-wise plane sweeping (D-PS) (Sec. 3.2) for allowing denser connections between 2D and stereo volumes.

Second, in Sec. 3.3, we compare the volume effectiveness for differently shaped objects between camera front-view and top-view. For aggregating more view-specific features, we introduce Dual-view Stereo Volume (DSV), which includes volumes integration and front-surface depth head.

Finally, in Sec. 3.4, we introduce a multi-modal data augmentation strategy – *Stereo-LiDAR copy-paste* for increasing the positive sample ratio and balancing the category distribution in 3D space.

#### 3.1 Stereo Volumes Generation Revisit

Given a binocular image pair  $(I_L, I_R)$ , the objective is to detect and localize objects in 3D world space. To avoid information loss of depth uncertainty in explicit data forms such as point clouds, recent approaches [23], [24] tend to create a stereo volume and encode the geometry cues into the 3D volume. With the geometric-guided cues, 3D object detection can be estimated accurately. In this section, we

briefly revisit several structures of stereo feature volumes – plane-sweep volume in the left camera frustum space and 3D-geometry volume (or BEV volume [24]) in 3D regular space.

For simplicity, we denote the voxel coordinate  $\mathbf{u} = (u, v, d)$  in camera frustum space and the voxel coordinate  $\mathbf{x} = (x, y, d)$ , where  $d$  denotes the depth dimension.  $proj : \mathbb{R}^3 \rightarrow \mathbb{R}^2$  represents the projection.

**Binocular Images to Plane-Sweep Volume.** The binocular features are generated by feeding a binocular image pair  $(I_L, I_R)$  into a Siamese network. In stereo matching [7], [29], [69] and MVS [30], [43], a set of evenly-spaced depth (or disparity) planes are generated towards the target view. By adopting the classic plane sweeping in the left camera view, multiplane images (MPI) [70] are generated by gathering image features at each depth plane. The per-view mapping function can be formulated as

$$PSV : \mathbb{R}^{H_I \times W_I \times C_I} \rightarrow \mathbb{R}^{H_V \times W_V \times D_V \times C_V}, PSV(\mathbf{I}) = \mathbf{V}_{proj}$$

where  $\mathbf{V}_{proj}(\mathbf{u}, c) = \mathbf{I}(proj(\mathbf{u}), c)$ . (1)

where voxels with coordinates  $\{\mathbf{x} = (u, v, d)\}_{PSV}$  are uniformly spaced in the camera frustum with  $C_V$  ( $C_V = C_I$ ) channels. By matching feature similarity within each voxel, a neural network can infer the underlying 3D geometry at the target view.

**Plane-Sweep Volume to 3D-Geometry Volume.** As the final objective is to detect 3D objects in 3D world space, one way to encode the scene in the 3D world is to transform PSV to 3DGV. Specifically, a detection area of size  $(H_V, W_V, D_V)$  can be discretized into voxel grid. 3D-geometry volume is computed by reversing 3D projection from camera frustum space to 3D world space.

**Binocular Images to 3D-Geometry Volume.** Another way to construct 3D-geometry volume (or BEV volume [24]) is introduced by the operation of *differentiable unprojection* [43]. The discrete grid  $\{(x, y, z)\}_{3DGV}$  obtains the projected 2D image features at  $(u, v)$  by *differentiable bilinear sampling*. Image features of different views are aggregated as the voxel.

#### 3.2 Depth-wise Plane Sweeping for 2D-to-3D Transformation

3D volume construction from the images is critical to represent a 3D scene for either monocular or multi-view settings. It facilitates a series of downstream 3D applications, e.g., stereo matching, novel view synthesis, and 3D object detection. Without loss of generality, for a predefined voxel grid of size  $(H_V, W_V, D_V)$  in arbitrarily voxelized space, we retrieve multi-view features by the per-view projection of each voxel coordinate  $\mathbf{p} = (x, y, z)$ . In this way, volume construction  $\mathbf{V}$  from a specific view is formulated as

$$\mathbf{V} : \mathbb{R}^{H_I \times W_I \times C_I} \rightarrow \mathbb{R}^{H_V \times W_V \times D_V \times C_V}, \mathbf{V}(\mathbf{I}) = \mathbf{V}_{proj}$$

where  $\mathbf{V}_{proj}(\mathbf{p}, c) = \mathbf{I}(proj(\mathbf{p}), c)$ . (2)

where the 2D feature has the shape of  $(H_I, W_I, C_I)$ .

**2D-To-3D Modeling Bottleneck.** During the construction of stereo volume, an evident fact is that the extra dimension orthogonal to camera planes is generated. Normally, the feature grids are filled by replication of image features



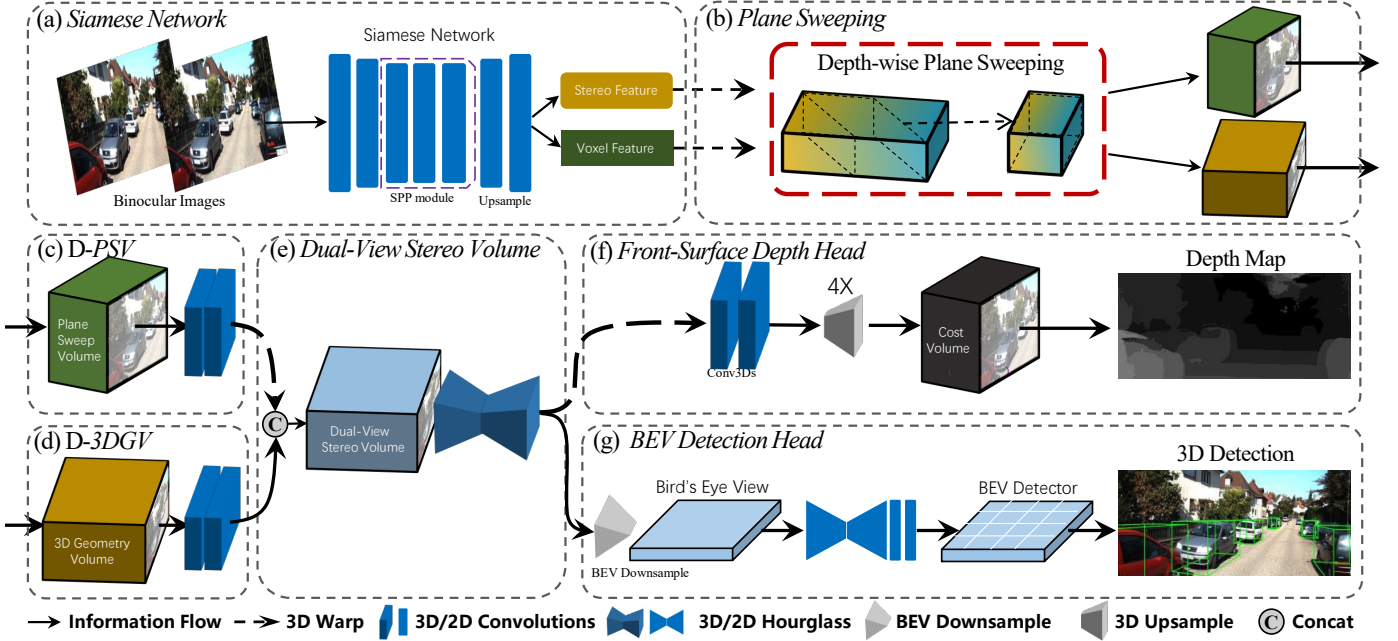


Fig. 1: **Overview of the proposed DSGN++ framework.** The whole framework consists of 6 components. (a) 2D image extraction network for extracting stereo features. (b) Volume construction process by Depth-wise Plane Sweeping. (c) 3D CNN for front-view feature extraction in the camera frustum space. (d) Flow integration followed by 3D CNN. (e) Depth head network that supervises depth signals in the front-view. (f) 3D detection head that detects objects in bird’s eye view.

through viewing rays. The size of generated 4D tensor  $\mathbf{V}$  is normally far larger than the source 2D feature tensor, expressed as

$$H_V \times W_V \times D_V \times C_V \gg H_I \times W_I \times C_I. \quad (3)$$

In prior stereo networks [6], [7], the number of depth planes ( $D_V$ ) is usually large, *e.g.*, 192-D and the feature resolution is maintained at least a quarter of the full resolution for matching at the pixel level. In other words, the representation power (a.k.a. effective degree of freedom [71], [72]) of the constructed 3D volume is constrained by its narrow 2D feature (small feature channels).

An ideal way for building a denser connection is to expand the channel size  $C_I$  of 2D feature map, which reduces the tensor dimension gap. However, expanding  $C_V$  is not straightforward as expanding volume channels  $C_V$  leads to more calculations in 3D. More, the transformation needs to maintain *feature locality* for matching the left-right correspondence cost.

Accordingly, we introduce the depth-wise (disparity-wise) plane sweeping (D-PS) to build a denser connection between 2D features and 3D volumes. Instead of compressing 2D feature channels to a small number, we preserve the number of channels  $C_I$  at a relatively large number (*e.g.*, 96) and slice the feature via a sliding window ( $C_V$  channels) along the channel axis. The shift on the channel axis depends on pixel disparity (inverse depth) as that distant object recognition is sensitive to sub-pixel differences. We empirically show in Sec. 4.3.1 that overcoming this challenge leads to considerable performance gain.

However, directly slicing the feature by shift produces unstable features as the order of feature channels is unchangeable. Therefore, we propose *Cyclic Slicing* to ensure

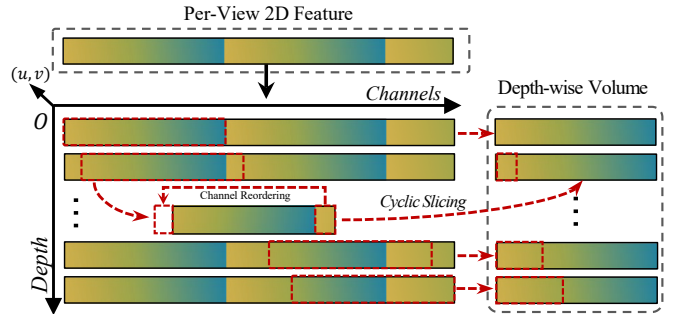


Fig. 2: **Depth-wise plane sweeping.** Assume the constructed volume is a 4D tensor in the space along  $(x, y, depth, channel)$  axes. We visualize the *depth-channel* plane of 3D featured volume where the graduated color indicates channel orders. Depth-wise volume is constructed by jointly sweeping the depth planes and slicing the features along the channel dimension. *Cyclic slicing* reorders the channels to ensure channel consistency across nearby depth planes.

local feature similarity for adjacent objects, *i.e.*, reordering the channels of the sliced features to maintain channel consistency.

**Cyclic Slicing.** Given a voxel coordinate  $\mathbf{x} = (x, y, d)$ , with its image feature channel  $C_I$ , we obtain the feature slice with  $C_V$  ( $C_V \leq C_I$ ) channels as the voxel feature. As shown in Fig. 2, we divide the  $C_I$  channels into several parts. Each region contains  $C_V$  channels except the last part. The sliced channels are an *ordered* union of two channel intervals of

$$[[\text{disp}/C_V] \times C_V, \text{disp} + C_V) \cup [\text{disp}, [\text{disp}/C_V] \times C_V)$$

where  $\lceil \cdot \rceil$  is the ceiling function. The reordering of the selected channels ensures feature continuity around nearby depth planes. For simplicity, we ignore cyclic slicing in Eqs. (4) and (5). The way to generate depth-wise plane-sweep volume ( $\mathbf{D-PSV}$ ) is expressed as

$$\begin{aligned} \mathbf{D-PSV} &: \mathbb{R}^{H_I \times W_I \times C_I} \rightarrow \mathbb{R}^{H_V \times W_V \times D_V \times C_V} \\ \mathbf{D-PSV}(\mathbf{I}) &= \mathbf{V}_{\text{proj}} \end{aligned} \quad (4)$$

where

$$\mathbf{V}_{\text{proj}}(\mathbf{u}, c) = \mathbf{I} \left( \text{proj}(\mathbf{u}), \left\lfloor \frac{f_u \times \text{baseline}}{d} \right\rfloor \mathbf{s} + c \right).$$

$\mathbf{s}$  is the ratio between 2D feature channels  $C_I$  and the number of depth planes  $D$ .  $\mathbf{u}$  denotes the coordinate  $(u, v, d)$  in the camera frustum.  $\alpha$  controls the smoothness of channel shifting rate.  $f_u$  denotes horizontal focal length and  $\text{baseline}$  denotes stereo camera baseline. Similarly, construction of depth-wise 3D-geometry volume ( $\mathbf{D-3DGV}$ ) is formulated as

$$\begin{aligned} \mathbf{D-3DGV} &: \mathbb{R}^{H_I \times W_I \times C_I} \rightarrow \mathbb{R}^{H_V \times W_V \times D_V \times C_V} \\ \mathbf{D-3DGV}(\mathbf{I}) &= \mathbf{V}_{\text{proj}} \end{aligned} \quad (5)$$

where

$$\mathbf{V}_{\text{proj}}(\mathbf{x}, c) = \mathbf{I} \left( \text{proj}(\mathbf{x}), \left\lfloor \frac{f_u \times \text{baseline}}{d} \right\rfloor \mathbf{s} + c \right).$$

where  $\mathbf{x}$  denotes the 3D coordinate  $(x, y, z)$ .

The computation complexity is exactly *same* as classic plane sweeping despite the growth of memory usage (the expansion of 2D feature map size). Experiments show that the simple solution to reduce the bottleneck leads to a considerable performance boost without extra techniques.

### 3.3 Dual-view Stereo Volume for Building Effective 3D Representation

In this section, we compare the information flows of two main pipelines in recent works [23], [24], [26], [65] as shown in Fig. 3 (a, b) and analyze the difference of their voxel shapes. Further, to more effectively represent depth and semantics, we introduce a new stereo volume – Dual-view Stereo Volume (DSV), that is susceptible to both views. This volume construction contains two key steps: *Volume Integration* and *Front-Surface Depth Head*.

**Front-view Representation vs. Top-view Representation.** In geometric learning, the front-view (FV) pipeline adopts plane-sweep volume for front-view depth learning in the camera frustum. Differently, the top-view (TV) pipeline constructs 3D structure within 3D-geometry volume (3DGV) in 3D regular space. The essential difference between the stereo volumes lies in their different shaped voxels or spaces, which directly leads to diverse receptive fields and voxel occupancy densities. Hence, taking KITTI dataset [32] as an example, we visualize average voxel occupancy counts for all categories and their performance in Fig. 4. Visually, nearby objects in PSV occupy much more voxels than faraway objects while the 3DGV curve is smoother. However, the average voxel occupancy counts for *Pedestrian* and *Cyclist* ( $< 20\text{m}$ ) are less than 100 voxels. The limited voxel occupancy hinders effective gradients towards the smaller objects, leading to the performance reduction on

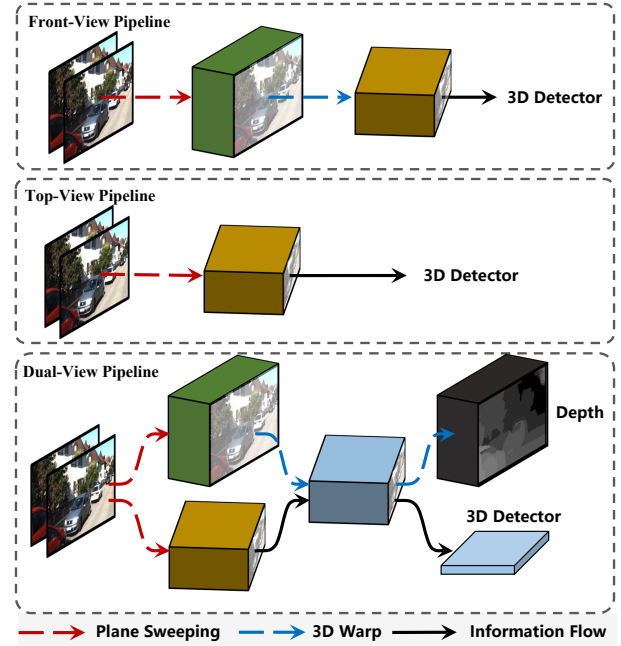


Fig. 3: **Comparison of stereo information flows.** Prior stereo detectors adapt 2D features to plane-sweep volume (green cube) or 3D-geometry volume (golden cube). Differently, dual-view stereo volume (DSV) aggregates both spaced features in 3D space and enforces geometric learning in the front view that is fit for visual sensors.

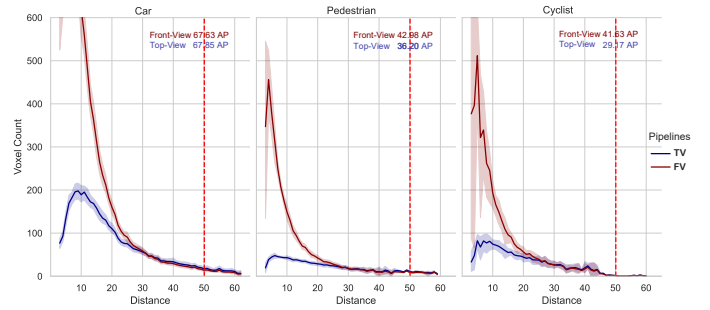


Fig. 4: **Comparison of average voxel occupancy per category within the plane-sweep and 3D-geometry volumes.** We set the maximum voxel numbers to 600 for visualization of distant regions.

3DGV. On the other hand, the distribution in PSV volume can deteriorate the learning of distant objects.

**Stereo Volumes Integration.** After construction of  $\mathbf{D-PSV}$  and  $\mathbf{D-3DGV}$ , we aggregate both information flows in our framework. Integration of both volumes allows the voxel to aggregate differently spaced 3D structure information and further expand the 2D-to-3D information flow. Specifically, we transform  $\mathbf{D-PSV}$  to 3D space and concatenate both volumes followed by a 3D Hourglass module [6]. The diversely spread voxel features are accessible within the combined feature volume. Experiments demonstrate the joint flows perform better than each independent volume under strong augmentation.

**Front-Surface Depth Head.** Geometric learning determines

the perception accuracy of distant scenes. DSGN [23] intermediately supervised the depth inside plane-sweep volume followed by the transformation to 3D-geometry volume that cannot efficiently encode geometric cues for the following 3D/BEV networks. PLUME [24] supervised the occupancy loss in 3D space that discretized the accurate depth values, which is inferior to reason the geometry as shown in experiments (Sec. 4.3.1).

To perceive the accurate front-surface structure, the depth head of stereo volume in 3D space (e.g., DSV) is firstly transformed to the camera frustum and applied by front-view depth map supervision. Meanwhile, the semantic supervision (e.g. 3D bounding boxes) indeed jointly act on the same feature volume. In detail, the 3D transformation starts by building the 3D coordinate mapping from camera frustum space to 3D space. With the coordinate mapping, voxels at  $(u, v, d)$  of the constructed camera obtain features  $(x, y, z)$  of the volume:

$$\begin{pmatrix} u \\ v \\ 1 \end{pmatrix} d = \begin{pmatrix} f_u & 0 & c_u \\ 0 & f_v & C_V \\ 0 & 0 & 1 \end{pmatrix} \begin{pmatrix} x \\ y \\ z \end{pmatrix}. \quad (6)$$

where  $f_u, f_v$  are the horizontal and vertical focal lengths. This generated front-view volume has the identical shape of PSV and is followed by a upsampling head network. The head network includes one hidden 3D convolution and a convolution that squeeze the channels to 1. The generated cost volume is then upsampled to original image size and supervised with depth loss [23], [27]. The construction enables mono-peak front-view depth that coincides with the real depth sensor data. Note that the transformation-based depth head is pluggable and can be inserted to 3D-geometry volume for both monocular and stereo settings.

### 3.4 Stereo-LiDAR Copy-Paste for Improving Data Efficiency

We illustrate the necessities to augment more and balanced foreground objects into the training scene as follows:

**Limited Foreground Area Ratio in Top View.** The 2D-to-3D transformation reduces the problem of front-view 3D detection to BEV detection. However, the foreground region ratio is also reduced in the bird’s eye view. The imbalance decreases the magnitude of foreground gradients back to the 2D network, leading to biased model learning.

**Imbalanced Class Distribution.** Long-tailed distribution commonly exists [73] in real scenes. For example, *pedestrian* and *cyclist* exists in less than 1/3 of full data, direct training of the imbalanced data could bias the gradient flow.

Unlike point clouds, multi-modal data augmentation is constrained by the tight correspondence between image and point clouds. For the localization of 3D objects, the *sub-pixel misalignment* affects the estimation of stereo disparity, leading to the large localization error for distant objects. Common copy-paste [31] randomly pastes object patches onto 2D images, which makes it hard to satisfy the projective constraint. Moreover, the segmentation mask is unavailable in binocular images and it is hard to guarantee the left-right alignment at pixel-level without human annotations.

To effectively augment the stereo data at the instance level, for the first time in literature, we propose a multi-modal data editing strategy – *Stereo-LiDAR copy-paste*

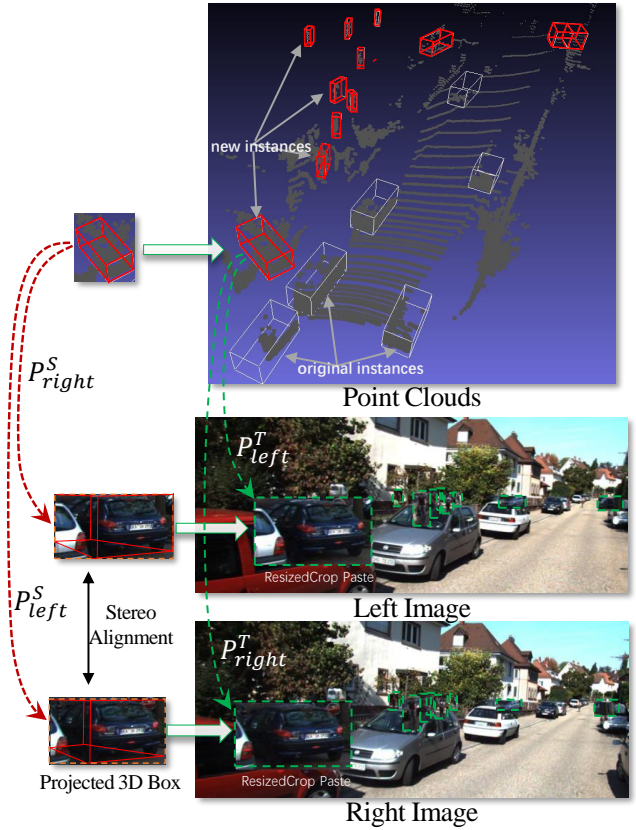


Fig. 5: **Joint Stereo-LiDAR copy-paste strategy.** For binocular training samples, the source object patches are cropped with their calibrated projections  $\{P_{left}^S, P_{right}^S\}$ . The augmented scene uses projections  $\{P_{left}^T, P_{right}^T\}$ . Object patches are pasted bilinearly to binocular images.

(SLCP) that maintains precise cross-modal alignments at the *sub-pixel* level. Specifically, we preserve the 3D location of the source objects and project the 3D boxes onto images with the target camera’s internal parameters. As shown in Fig. 5, suppose we sample several objects from their source scene for a target training scene. The cropped point clouds within objects can be put into the training scene. For binocular training images, we compute the projected 2D bounding box  $\mathbf{B}_S$  for each 3D object box  $\mathbf{B}_{3D}$  by the source projection matrices  $\{P_{left}^S, P_{right}^S\}$ . By projecting the same 3D box by target projection  $\{P_{left}^T, P_{right}^T\}$ , we obtain the target bounding box  $\mathbf{B}_T$ . We crop and warp the source object image patches to the respective target boxes as  $\mathbf{B}_S \rightarrow \mathbf{B}_T$ . Note stereo alignment still holds under horizontal flipping. In this way, the alignment between LiDAR and both stereo images is guaranteed at the sub-pixel level. Also, to ensure *uni-peak* depth, the overlapped 3D points, whose projections are within  $\mathbf{B}_T$ , are removed.

For a training scene, we sample a sufficient and balanced number of objects per category (5 objects per category) from other data and paste objects to the multi-modal data. Experiments demonstrate that our strategy effectively improves data efficiency and largely mitigates the imbalanced class distributions.



Sensor	Methods	Source	Car AP <sub>3D</sub>			Car AP <sub>BEV</sub>			Car AP <sub>2D</sub>		
			Easy	Mod.	Hard	Easy	Mod.	Hard	Easy	Mod.	Hard
LiDAR	SECOND [21]	Sensors2018	83.34	72.55	65.82	89.39	83.77	78.59	–	–	–
	Point R-CNN [20]	CVPR2018	86.96	75.64	70.70	92.13	87.39	82.72	94.00	91.90	88.17
	MV3D [49]	CVPR2017	74.97	63.63	54.00	86.62	78.93	69.80	–	–	–
	AVOD [33]	IROS2018	76.39	66.47	60.23	89.75	84.95	78.32	95.17	89.88	82.83
	PL++: P-RCNN +SL* [19]	ICLR2020	68.38	54.88	49.16	84.61	73.80	65.59	94.95	85.15	77.78
Stereo	TLNet [13]	CVPR2019	7.64	4.37	3.74	13.71	7.69	6.73	76.92	63.53	54.58
	Stereo-RCNN [8]	CVPR2019	47.58	30.23	23.72	61.92	41.31	33.42	93.98	85.98	71.25
	PL: AVOD [17]	CVPR2019	54.53	34.05	28.25	67.30	45.00	38.40	85.40	67.79	58.50
	ZoomNet [74]	AAAI2020	55.98	38.64	30.97	72.94	54.91	44.14	94.22	83.92	69.00
	PL++: P-RCNN [19]	ICLR2020	61.11	42.43	36.99	78.31	58.01	51.25	94.46	82.90	75.45
	OC-Stereo [64]	ICRA2020	55.15	37.60	30.25	68.89	51.47	42.97	87.39	74.60	62.56
	Disp R-CNN [75]	CVPR2020	68.21	45.78	37.73	79.76	58.62	47.73	93.45	82.64	70.45
	DSGN [23]	CVPR2020	73.50	52.18	45.14	82.90	65.05	56.60	95.53	86.43	78.75
	CDN (DSGN) [67]	NeurIPS2020	74.52	54.22	46.36	83.32	66.24	57.65	95.85	87.19	79.43
	CG-stereo [76]	IROS2020	74.39	53.58	46.50	83.32	66.44	58.95	96.31	90.38	82.80
	YoLoStereo3D [77]	AAAI2021	65.68	41.25	30.42	76.10	50.28	36.86	94.81	82.15	62.17
	PLUME-Middle [24]	ICRA2021	–	–	–	83.0	66.3	56.7	–	–	–
	LIGA [27]	ICCV2021	81.39	64.66	57.22	88.15	76.78	67.40	96.43	93.82	86.19
	DSGN++ (Ours)	–	<b>83.21</b>	<b>67.37</b>	<b>59.91</b>	<b>88.55</b>	<b>78.94</b>	<b>69.74</b>	<b>98.08</b>	<b>95.70</b>	<b>88.27</b>

TABLE 1: Performance comparison on the official KITTI test server (Car). \* means refining the pseudo point clouds by additional 4-beam LiDAR. Best results are highlighted in bold.

## 4 EXPERIMENTS

In this section, we conduct extensive experiments to validate the effectiveness of our proposed framework with the settings of various modalities. In Sec. 4.1, we briefly illustrate the datasets and experimental setups for 3D object detection. The quantitative and qualitative results are provided in Sec. 4.2 and Sec. 4.4, respectively. We further illustrate the usefulness of each component in the ablation study (Sec. 4.3.1). Lastly, the efficiency of our approach is discussed in Sec. 4.5.

### 4.1 Experimental Setup

**Datasets.** We evaluate methods on the popular KITTI 3D object detection dataset [32], which is a union of 7,481 stereo image-pairs and point clouds for training and 7,518 for testing. The training data has annotations for *Car*, *Pedestrian* and *Cyclist*. The ground-truth depth maps are generated from point clouds following [17], [19], [23]. Following the protocol in [23], [49], the training data is divided into a training set (3,712 images) and a validation set (3,769 images). As KITTI leaderboard limits the access to submission to the server for evaluating the test set, the ablation studies are conducted on the KITTI *train-val* split.

**Evaluation Metric.** KITTI divides the evaluation metric into three regimes (Easy, Moderate, and Hard) according to their recognition difficulty, which considers object occlusion/truncation and the size of an object in the 2D image. The AP evaluations for 2D, BEV and 3D have diverse IoU criteria per class, *i.e.*,  $\text{IoU} \geq 0.7$  for *Car*,  $\text{IoU} \geq 0.5$  for *Pedestrian* and *Cyclist*. All experiments and ablation studies adopt  $AP|_{R40}$  by default as the KITTI benchmark altered AP calculation that utilizes 40 recall positions ( $AP|_{R40}$ ) instead of the earlier 11 recall positions ( $AP|_{R11}$ ).

**Experimental Setups.** Our models are trained with the respectively best-performing parameters in four NVIDIA V100 GPUs, each GPU holds one pair of stereo images of size  $384 \times 1248$ . We apply ADAM [78] optimizer with

initial learning rate 0.001. Data augmentation strategy [23] includes horizontal flipping and *Stereo-LiDAR copy-paste*. All models are trained for 60 epochs and the learning rate is decreased by 10 at the 50-th epoch.

**Baseline Methods.** We build our framework based on the official author-released codes – DSGN [23] and LIGA [27], [79]). LIGA improves DSGN with several technical modifications and provides a stronger baseline approach. Based on the LIGA-version DSGN, we further make several modifications for efficient implementation and adopt it (called L-DSGN) as the baseline approach unless otherwise specified. Particularly, we set the kernel size to  $1 \times 1 \times 1$  for all the first 3D convolution after stereo volumes and move the 3D hourglass network after Dual-view Stereo Volume as shown in Fig. 1. Also, as depth-wise plane sweeping supports wider feature inputs, L-DSGN aggregates the multi-scale features by concatenation for binocular feature extraction instead of feature addition. The last 2D convolution layer uses the number of filters  $C_I$  according to the type of plane sweeping. During testing, the 2D detection head and depth prediction head are dropped. Synchronized batch normalization is applied throughout the network.

**Implementation of Stereo Volumes.** PSV is pre-defined with shape  $(W_I/4, H_I/4, D_I/4, 64)$ , where the image size is  $(W_I = 1248, H_I = 384)$ . Both left and right image features are with 32 channels. The number of depth  $D_I$  is set to 192 (DSGN) and 288 (L-DSGN). Extra 3D convolutions are applied to squeeze the channel dimension to 32-D. 3DGV contains a 3D voxel occupancy grid of size  $(W_V = 300, H_V = 20, D_V = 288)$  along the respective directions in KITTI camera’s view with each voxel of size  $(0.2, 0.2, 0.2)$  (meters). Extra 3D convolutions with 32 filters for compressing the features when generating 3DGV  $(H_V \times W_V \times D_V \times 64)$  directly from binocular images. Both stereo volumes adapt the 2D semantic features by plane-sweeping. We set the shifting ratio  $\alpha$  of Depth-wise plane sweeping to 0.1 and its input channels  $C = 96$  by default.

Sensor	Methods	Source	Ped. AP <sub>3D</sub>			Ped. AP <sub>BEV</sub>			Cyc. AP <sub>3D</sub>			Cyc. AP <sub>BEV</sub>		
			Easy	<b>Mod</b>	Hard	Easy	<b>Mod</b>	Hard	Easy	<b>Mod</b>	Hard	Easy	<b>Mod</b>	Hard
LiDAR	Point R-CNN [20]	CVPR2018	47.98	39.37	36.01	54.77	46.13	42.84	74.96	58.82	52.53	82.56	67.24	60.28
	AVOD [33]	IROS2018	36.10	27.86	25.76	42.58	33.57	30.14	57.19	42.08	38.29	64.11	48.15	42.37
Stereo	OC-Stereo [64]	ICRA2020	24.48	17.58	15.60	29.79	20.80	18.62	29.40	16.63	14.72	32.47	19.23	17.11
	Disp R-CNN [75]	CVPR2020	37.12	25.80	22.04	40.21	28.34	24.46	40.05	24.40	21.12	44.19	27.04	23.58
	DSGN [23]	CVPR2020	20.53	15.55	14.15	26.61	20.75	18.86	27.76	18.17	16.21	31.23	21.04	18.93
	CG-stereo [76]	IROS2020	33.22	24.31	20.95	39.24	29.56	25.87	47.40	30.89	27.73	55.33	36.25	32.17
	YoLoStereo3D [77]	AAAI2021	28.49	19.75	16.48	31.01	20.76	18.41	–	–	–	–	–	–
	LIGA [27]	ICCV2021	40.46	30.00	27.07	44.71	34.13	30.42	54.44	36.86	32.06	58.95	40.60	35.27
	DSGN++ (Ours)	–	<b>43.05</b>	<b>32.74</b>	<b>29.54</b>	<b>50.26</b>	<b>38.92</b>	<b>35.12</b>	<b>62.82</b>	<b>43.90</b>	<b>39.21</b>	<b>68.29</b>	<b>49.37</b>	<b>43.79</b>

TABLE 2: Performance comparison on the official KITTI test server (Pedestrian and Cyclist). Best results are highlighted in bold.

Methods	Car			Pedestrian			Cyclist		
	AP <sub>3D</sub>	AP <sub>BEV</sub>	AP <sub>2D</sub>	AP <sub>3D</sub>	AP <sub>BEV</sub>	AP <sub>2D</sub>	AP <sub>3D</sub>	AP <sub>BEV</sub>	AP <sub>2D</sub>
<i>LiDAR Sensor</i>									
SECOND [21], [79]	78.62	87.93	89.90	52.98	56.66	66.33	67.15	70.70	77.09
PV-RCNN [80]	84.43	94.03	89.44	54.89	58.14	65.37	71.52	75.31	83.04
<i>Stereo Camera Sensor</i>									
DSGN [23] †	56.09	65.24	85.03	35.39	42.58	55.22	25.37	27.43	35.3
ours, DSGN++ on DSGN †	61.62	70.61	89.47	<b>44.17</b>	48.51	62.35	36.04	39.05	43.56
<i>Improvement</i>	<b>+5.53</b>	<b>+5.37</b>	<b>+4.44</b>	<b>+8.78</b>	<b>+5.93</b>	<b>+7.13</b>	<b>+10.67</b>	<b>+11.62</b>	<b>+8.26</b>
L-DSGN	63.58	73.53	93.59	33.12	40.50	59.16	28.09	29.58	36.95
ours, DSGN++ on L-DSGN	<b>69.12</b>	<b>78.93</b>	<b>95.85</b>	42.44	<b>50.06</b>	<b>68.92</b>	<b>42.48</b>	<b>45.77</b>	<b>53.81</b>
<i>Improvement</i>	<b>+5.54</b>	<b>+5.40</b>	<b>+2.26</b>	<b>+8.32</b>	<b>+8.56</b>	<b>+9.76</b>	<b>+14.39</b>	<b>+16.19</b>	<b>+16.86</b>
<i>Multi-Modal Sensors</i>									
4-LiDAR SECOND4x	23.82	30.85	32.27	16.70	21.79	24.85	12.18	13.45	14.05
Fusion with DSGN++	67.41	76.30	95.17	40.85	49.51	62.65	32.31	33.69	46.17
<i>Improvement</i>	<b>+43.59</b>	<b>+45.45</b>	<b>+62.90</b>	<b>+24.15</b>	<b>+27.72</b>	<b>+37.80</b>	<b>+20.13</b>	<b>+20.24</b>	<b>+32.12</b>
8-LiDAR SECOND4x	49.00	66.83	66.97	38.19	44.34	44.13	25.88	27.56	31.17
Fusion with DSGN++	78.15	85.49	95.48	51.03	59.48	71.58	46.83	48.25	53.23
<i>Improvement</i>	<b>+29.15</b>	<b>+18.66</b>	<b>+28.51</b>	<b>+12.84</b>	<b>+15.14</b>	<b>+27.45</b>	<b>+20.95</b>	<b>+20.69</b>	<b>+22.06</b>
16-LiDAR SECOND4x	65.31	78.28	80.18	52.97	58.62	59.40	43.86	47.37	49.35
Fusion with DSGN++	79.41	87.55	95.17	58.07	66.18	74.55	54.08	55.95	59.63
<i>Improvement</i>	<b>+14.10</b>	<b>+9.27</b>	<b>+14.99</b>	<b>+5.10</b>	<b>+7.56</b>	<b>+15.15</b>	<b>+10.22</b>	<b>+8.58</b>	<b>+10.28</b>
64-LiDAR SECOND4x	81.23	89.52	94.37	59.40	62.71	68.50	61.90	62.45	68.87
Fusion with L-DSGN	81.13	88.36	94.50	60.05	62.65	68.42	56.94	57.05	65.84
Fusion with DSGN++	<b>85.32</b>	<b>91.37</b>	<b>95.79</b>	<b>63.03</b>	<b>68.87</b>	<b>76.72</b>	<b>63.79</b>	<b>66.18</b>	<b>73.87</b>
<i>Improvement</i>	<b>+4.09</b>	<b>+1.85</b>	<b>+1.42</b>	<b>+3.63</b>	<b>+6.16</b>	<b>+8.22</b>	<b>+1.89</b>	<b>+3.73</b>	<b>+5.00</b>

TABLE 3: Performance comparison on the KITTI val set in various modality settings. Results in moderate difficulty regime for all categories are provided as the main metric. † means training another model for Pedestrian and Cyclist. Best results are highlighted in bold for each sensor setup.

## 4.2 Quantitative Results

### 4.2.1 Official Results on the KITTI test benchmark

We report experimental results with comparison on the KITTI test set as shown in TABLE 1 and TABLE 2. Without cross-modal distillation [27], [68], the simple solution DSGN++ outperforms all other stereo-based approaches over all difficulties and evaluation metrics (Car: **+2.71** AP<sub>3D</sub>, **+2.16** AP<sub>BEV</sub>, and **+1.88** AP<sub>2D</sub> in moderate difficulty regime). In terms of AP<sub>2D</sub>, our approaches achieve the impressively high **95.70** AP, surpassing all the strong 3D object detectors.

As detecting smaller and non-rigid 3D objects pose the greater challenge for the regime of camera-based 3D detectors, only several approaches report the results for

Pedestrian and Cyclist. To verify the generalization ability of our approach, we provide the results of Pedestrian and Cyclist in TABLE 2. Our approach achieves noticeable improvements over prior methods (Cyc.: **+7.04** AP<sub>3D</sub>, Ped.: **+2.74** AP<sub>3D</sub>).

Compared with LiDAR-based approaches, in terms of AP<sub>3D</sub>, our method even completely beats some LiDAR detectors including AVOD for all categories (for the first time in literature). Concretely, DSGN++ exceeds AVOD by 5.82 AP<sub>2D</sub> in the front view while scoring 6.01 AP<sub>BEV</sub> lower than AVOD in the bird’s eye view. This comparison indicates that the performance between camera-based approaches mainly lies in the foreground depth estimation error.



id.	Pipelines	FSD Head	D-PS	SLCP	Car		Pedestrian		Cyclist	
					AP <sub>3D</sub>	AP <sub>BEV</sub>	AP <sub>3D</sub>	AP <sub>BEV</sub>	AP <sub>3D</sub>	AP <sub>BEV</sub>
a.	Front-View	✓			63.58	73.53	33.12	40.50	28.09	29.58
b.		✓	✓		66.42	77.13	34.91	41.76	30.17	34.29
c.		✓	✓	✓	67.63	76.73	<b>42.98</b>	<b>50.64</b>	41.63	43.96
d.	Top-View				56.69	66.05	28.23	32.08	18.59	17.47
e.		✓			61.33	71.45	29.14	35.02	20.51	19.71
f.		✓	✓		64.59	74.14	29.38	39.12	20.45	21.28
g.		✓	✓	✓	67.85	77.16	36.20	43.09	29.17	30.56
h.	Dual-View				61.46	67.81	33.41	40.59	23.42	24.74
i.		✓			64.43	74.19	33.51	42.48	33.82	35.64
j.		✓	✓		66.21	76.96	37.19	44.50	30.01	32.69
k.		✓	✓	✓	<b>69.12</b>	<b>78.93</b>	42.44	50.06	<b>42.48</b>	<b>45.77</b>

TABLE 4: **Main ablation studies on the KITTI *val* set.** As illustrated in Fig. 3, we separate the pipelines according to the information flow types – front-view (FV), top-view (TV), and dual-view (DV). FSD Head denotes the application of front-surface depth head (Sec. 3.3) for geometric learning. SLCP represents *Stereo-LiDAR copy-paste*. Originally FV applies depth head and TV is supervised by voxel occupancy loss. “–” denotes the component is not applicable in the respective pipeline.

#### 4.2.2 Method Performance in Stereo Setup

As shown in TABLE 3, we build our model based on two networks DSGN [23] (PSMNet [6] backbone) and L-DSGN [27] (ResNet-34 backbones). We adopt the same experimental settings for the respective experiments. By incorporating the proposed techniques, our method significantly surpasses the baselines: DSGN (Car: +5.53 AP<sub>3D</sub>, Ped.: +8.78 AP<sub>3D</sub>, Cyc.: +11.67 AP<sub>3D</sub>) and L-DSGN (Car: +5.54 AP<sub>3D</sub>, Ped.: +8.32 AP<sub>3D</sub>, Cyc.: +16.19 AP<sub>3D</sub>) regarding the moderate evaluation difficulty. The more noticeable improvements for *Pedestrian* and *Cyclist* reveal that the imbalanced class learning is greatly alleviated.

#### 4.2.3 Method Performance in Multi-Modal Setup

We further validate the effectiveness of our approaches in the multi-modal setting – binocular cameras and LiDAR. The adopted LiDAR baseline network is SECOND4x [21], [27], which downsamples sparse grid by 4 times in the bird’s eye view and has the same grid size with stereo volume. Without special design, we simply fuse the learned Dual-view Stereo Volume by feature addition with LiDAR feature volume generated by SECOND4x. This multi-modal modeling uses the same training setup as in Sec. 4.1.

We conduct a set of experiments that inputs LiDAR signals from sparse (4 beams) to dense (complete 64 beams) to validate the complementary effects by stereo cameras. The low-beams simulation of LiDAR signals follows [19]. As shown in TABLE 3, SECOND4x cannot handle well with the low-beams LiDAR and gets only  $< 50$  AP<sub>3D</sub> with inputs of  $\leq 8$ -beams LiDAR. With the simple fusion above with stereo features, all the LiDAR networks obtain noticeable accuracy gain consistently. The sparser the LiDAR signal is, the better the acquired improvements are. For example, 8-beams LiDAR network gets an accuracy boost of 29.15 AP<sub>3D</sub> to 78.15 AP, which is even comparable to the reported results of SECOND with inputs of 64-beams LiDAR.

In particular for the complete 64-beams LiDAR setup, direct multi-modal modeling by fusing L-DSGN even deteriorates the detection performance. In contrast, multi-modal modeling with DSGN++ yet improves the LiDAR network

significantly (Car: +4.09 AP<sub>3D</sub>, Ped.: +3.63 AP<sub>3D</sub>, Cyc.: +1.89 AP<sub>3D</sub>). This comparison reveals the fact that stereo representation can provide strong complementary cues over the vanilla LiDAR signals. The fusion of multi-sensor is promising and improves the robustness of 3D perception system.

### 4.3 Ablation Study

In this section, we investigate the effectiveness of the major adaptations. For fair comparisons, we conduct ablation studies on the KITTI *val* set mainly in TABLE 4. Note that we primarily adopts the accuracy of *Car* category for the ablation study by default, as the dataset contains less annotations for *Pedestrian* and *Cyclist* that causes greater result variance.

#### 4.3.1 Ablation Study for Depth-wise Plane Sweeping

As shown in TABLE 4 (a. vs. b.; d. vs. e.; h. vs. i.), with similar computations, models with depth-wise plane sweeping obtains extra 1.5~3.2 AP improvements. In general, performance gains are consistent for all three categories, which indicates that traditional plane sweeping is unsuited for representing complicated predictions, and D-PS much eases it.

TABLE 5 ablates the expanded channels  $C_I$  and smoothness factor  $\alpha$  for plane sweeping. We observe that the wider 2D features contribute to the learning of 2D semantic features. We compare D-PS with another possible choice (called Group-PS) to input the features with expanded channels: equally splitting the channels/depths into several groups and extract the depth-wise features in the respective groups. However, Group-PS cannot guarantee feature’s channel-wise similarity between groups for stereo matching and yields 65.48 AP<sub>3D</sub>. D-PS is designed to preserve the local feature *continuity* and the degree of sharing can be adjusted w.r.t disparity. The smoothing factors  $\alpha = 0.1$  (66.42 AP<sub>3D</sub>) for FV and  $\alpha = 0.5$  (64.59 AP<sub>3D</sub>) for TV yield best performance. Dual-view stereo volume adopts the respective best-performing parameters for both volumes.

Pipelines	Sampling	#Chn	$\alpha$	Car	
				AP <sub>3D</sub>	AP <sub>BEV</sub>
<i>Stereo Camera Sensor</i>					
FV	PS	32	–	63.58	73.53
	Group-PS	96	32-sep	64.98	76.02
	D-PS	48	0.1	65.48	76.28
		96	1.	65.95	76.71
		96	0.1	<b>66.42</b>	<b>77.13</b>
96	0.01	66.28	76.82		
TV	PS	32	–	61.33	71.45
	Group-PS	96	32-sep	62.50	72.60
	D-PS	48	0.1	62.59	73.22
		96	1	63.85	73.59
		96	0.5	<b>64.59</b>	<b>74.14</b>
96	0.1	64.15	73.40		
<i>Monocular Camera Sensor</i>					
TV	PS	32	–	15.36	21.23
	D-PS	96	0.1	<b>17.41</b>	<b>24.04</b>

TABLE 5: Effects of expanded channels and smoothness factor  $\alpha$  for Depth-wise Plane Sweeping. #Chn denotes the channel number  $C_I$  of 2D feature for building volumes. “Group-PS” (32-sep) represents sweeping planes by propagates features from the evenly-spaced channel groups (each with 32 channels) to the depth planes of the respective group.

In addition, to illustrates the generality of D-PS, we also provide the monocular experiments. We simply adapt the top-view pipeline for monocular 3D detectors (remove right image input and right feature) and keep other training setups same. As shown in the bottom of TABLE 5, method with D-PS surpasses the baseline by 2.05 AP<sub>3D</sub> and 2.81 AP<sub>BEV</sub>.

#### 4.3.2 Ablation Study for Stereo Volumetric Representation

We conduct the comparison of several stereo pipelines (See information flows in Fig. 3)).

**Effects of Front-Surface Depth Head.** TABLE 4(d. vs. e., h. vs. i.) compares the effects of different depth supervision signals (voxel occupancy head vs. front-surface depth head), where FSD head yields the respective performance gains of Car: +4.64 AP<sub>3D</sub> and +2.97 AP<sub>3D</sub>. The improvement reveals that FSD head can take in more accurate depth signals that simple occupancy classification.

**Effects of Volume Integration.** For fair comparison of both single view representations, we ensure the front-view pipeline and top-view one shares similar volume sizes: PSV is of shape  $72 \times 80 \times 32 = 1797120$  and 3DGV has the shape of  $20 \times 304 \times 288 = 1751040$ , and there is only 2.6% calculation counts difference. As shown in TABLE 4 (c. vs. g.; b. vs. f.), despite the input of balanced foreground categories, TV branch cannot achieve the same performance for Ped. and Cyc., which shows top-view representation may not be well-suited for smaller objects in bird’s eye view. The volume integration (k. in TABLE 4) boosts the performance to (69.12 AP<sub>3D</sub>, 78.93 AP<sub>BEV</sub>) for Car, and (42.48 AP<sub>3D</sub>, 45.77 AP<sub>BEV</sub>) for Cyc.. In comparison of c., g. and k., top-view representation provides more complementary cues for Car and Cyc..

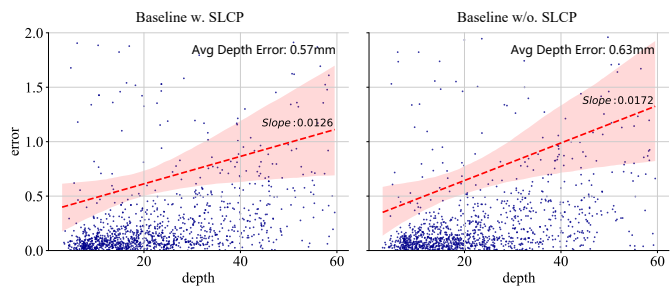


Fig. 6: Comparison of foreground object localization error. Red dotted line computes the regressed line. The localization error computes the average depth estimation error within the 3D object boxes at the respective depth ranges.

id.	Samples	Prob	Car	Ped.	Cyc.
a.	–	0.	66.21	37.19	30.01
b.	{3, 3, 3}	0.6	67.79	39.66	39.56
c.	{5, 0, 0}	0.6	68.74	32.50	28.81
d.	{0, 5, 5}	0.6	66.18	39.42	43.22
e.	{5, 5, 5}	0.4	68.79	39.20	<b>43.51</b>
f.		0.6	<b>69.12</b>	<b>42.44</b>	42.48
g.		0.8	68.41	41.74	39.47
h.	1.	68.55	40.18	38.58	
i.	{7, 7, 7}	0.6	68.92	41.03	42.93
j.	w/o Occ Removal		66.52	38.79	36.27

TABLE 6: Hyper-parameter choices for Stereo-LiDAR copy-paste. Models are evaluated using AP<sub>3D</sub> (Moderate) on the KITTI val set. “Samples” denotes the augmented object counts for Car, Pedestrian, and Cyclist, respectively. “Prob” indicates the apply SLCP for each training scene. “w/o Occ Removal” denotes cancelling the removal of occluded point clouds.

#### 4.3.3 Ablation Study for Stereo-LiDAR Copy-Paste

TABLE 4 (j. vs. k.) shows that SLCP augmentation improves data efficiency (Car: +3.96 AP<sub>3D</sub>) and greatly mitigates imbalanced class learning (Ped.: +5.25 AP<sub>3D</sub>, Cyc. +12.47 AP<sub>3D</sub>).

In terms of depth estimation quality, as visualized in Fig. 6, the foreground localization error w.r.t object distances gets a smoother slope. Overall, our model reduce the foreground depth estimation error from 0.63 to 0.57 (mm).

TABLE 6 ablates several hyper-parameters used in Stereo-LiDAR copy-paste. TABLE 6 (a., b., f., i.) ablates the number of inserted samples into the training scenes and 5 samples yield the best performance. TABLE 6 (a., c., d.) ablates the effect of more positive numbers, where the improvement of +2.53 AP<sub>3D</sub> for Car (TABLE 6 (a. vs. c.)) indicates that the current positive instances limit the modeling efficiency even if Car is the most common instance. (e. - h.) ablates the probability of applying copy paste. As the image-level copy paste produces object patch artifacts and occlusion, the larger probability can lead to worse results. TABLE 6(f. vs. j.) ablates whether to remove the background point clouds and the results reveal the removal of background points facilitates the model to better learn from copy-paste augmentation (Car: +2.60 AP<sub>3D</sub>).

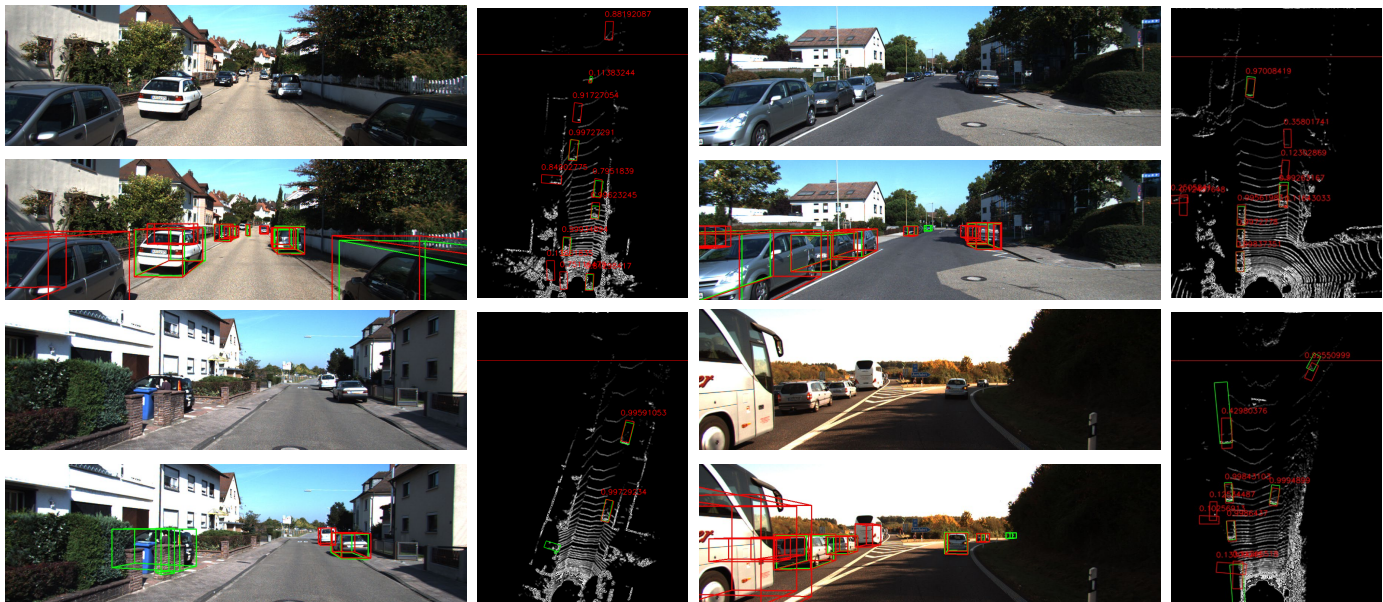


Fig. 7: **Qualitative results on the KITTI val set.** Green boxes represents ground-truth and red boxes denotes our predictions. The left-view images are shown in the left column and the BEV point clouds images are shown in the right side. Some failure cases are shown at the bottom of the table. Please zoom in to observe the prediction details. Red line shown in the bird’s eye view is 50 meters away from the sensor.

	Car AP <sub>3D</sub>	Car AP <sub>BEV</sub>	Inference Time
DSGN++	<b>69.12</b>	<b>78.93</b>	0.281s
FV-DSGN++	67.63	76.73	0.198s
TV-DSGN++	67.85	77.16	0.202s
R18-DSGN++	68.12	77.01	<b>0.178s</b>

TABLE 7: **Inference time comparison and the efficient implementation.** The experiments are conducted on a NVIDIA RTX 2080Ti GPU with batch size of 1.

#### 4.4 Qualitative Results

We present some representative results in Fig. 7, especially for the occlusion situations. From the visualization of BEV results, our approach robustly predicts most objects and estimates their accurate 3D bounding boxes even for the scene 50 meters away (red line in the bird’s eye view). The visualization shows the great potentials for the low-cost outdoor perception system based on stereo cameras. Noticeably, some extremely occluded cases in the top row could be still detected. The bottom row in Fig. 7 also visualizes some failure cases including missing occluded objects, missing distant objects, wrong orientation/dimension predictions.

#### 4.5 Efficiency Study

As the large performance gap between LiDAR-based approaches and camera-based approaches [24], [26], [27], most works focus on the improvement of detection accuracy. Efficiency comparison of different algorithms is less investigated due to various experimental setups.

For a fair comparison, we conduct the efficiency comparisons on an NVIDIA RTX 2080TI GPU as shown in TABLE 7. Generally, the complete DSGN++ with ResNet-34 runs takes 0.273s on average, where binocular feature

extraction takes  $2 \times 0.058 = 0.116$ s, PSV takes 0.036s, 3DGV takes 0.045s, DSV and 3D network take 0.044s and last BEV detector costs 0.012s. The inference time of single-view pipelines TV-DSGN++ and FV-DSGN++ are 0.198s and 0.202s, respectively.

For accelerating our pipeline, we provides another efficient implementation (R18-DSGN++) to demonstrate the speed-accuracy trade-off of our work. We replace ResNet-34 with ResNet-18 and adopt the same 2D upsampling head for both stereo volumes. The efficient model still achieves 68.12 AP<sub>3D</sub> despite the backbone network removing about half of the parameters. This fact also indicates that the original 2D backbone network is not fully exploited for the construction of the following stereo volumes as described in Sec. 3.2.

We note that the code is not yet fully optimized and affects the speed of the 3D detector. For example, despite the same computation, the CUDA implementation of *D-PS* costs extra 4ms than PyTorch built-in implementation of *F.grid\_sample* for plane sweeping. We leave the further code optimization to future work.

## 5 CONCLUSION

We have renewed several key components that build an end-to-end stereo detection pipeline and provided a new stereo modeling – DSGN++ – for 3D object detection. Without bells and whistles, we conducted a set of comprehensive experiments to illustrate the effectiveness of the proposed modules. Specifically, the proposed depth-wise plane sweeping allows inputs of wider 2D features and improves modeling efficiency in 2D-to-3D transformation. Dual-view stereo volumes provide better 3D representations that grasp differently spaced features. And *Stereo-LiDAR*



*copy-paste* strategy largely improves data efficiency and enhances modeling generalization ability for *all* categories. We expect the framework provides a strong baseline for the future application of camera-based 3D perception systems.

## REFERENCES

- [1] R. Girshick, J. Donahue, T. Darrell, and J. Malik, "Rich feature hierarchies for accurate object detection and semantic segmentation," in *CVPR*, 2014, pp. 580–587.
- [2] R. Girshick, "Fast r-cnn," in *ICCV*, 2015.
- [3] S. Ren, K. He, R. Girshick, and J. Sun, "Faster r-cnn: Towards real-time object detection with region proposal networks," in *NeurIPS*, 2015.
- [4] W. Liu, D. Anguelov, D. Erhan, C. Szegedy, S. Reed, C.-Y. Fu, and A. C. Berg, "Ssd: Single shot multibox detector," in *ECCV*, 2016.
- [5] H. Fu, M. Gong, C. Wang, K. Batmanghelich, and D. Tao, "Deep ordinal regression network for monocular depth estimation," in *CVPR*, 2018, pp. 2002–2011.
- [6] J.-R. Chang and Y.-S. Chen, "Pyramid stereo matching network," in *CVPR*, 2018, pp. 5410–5418.
- [7] A. Kendall, H. Martirosyan, S. Dasgupta, P. Henry, R. Kennedy, A. Bachrach, and A. Bry, "End-to-end learning of geometry and context for deep stereo regression," in *ICCV*, 2017, pp. 66–75.
- [8] P. Li, X. Chen, and S. Shen, "Stereo r-cnn based 3d object detection for autonomous driving," in *CVPR*, 2019, pp. 7644–7652.
- [9] Z. Qin, J. Wang, and Y. Lu, "Monogrnnet: A geometric reasoning network for monocular 3d object localization," in *AAAI*, vol. 33, 2019, pp. 8851–8858.
- [10] B. Xu and Z. Chen, "Multi-level fusion based 3d object detection from monocular images," in *CVPR*, 2018, pp. 2345–2353.
- [11] Y. Zhang, J. Lu, and J. Zhou, "Objects are different: Flexible monocular 3d object detection," in *CVPR*, 2021, pp. 3289–3298.
- [12] M. Ding, Y. Huo, H. Yi, Z. Wang, J. Shi, Z. Lu, and P. Luo, "Learning depth-guided convolutions for monocular 3d object detection," in *CVPR Workshops*, 2020, pp. 1000–1001.
- [13] Z. Qin, J. Wang, and Y. Lu, "Triangulation learning network: from monocular to stereo 3d object detection," *CVPR*, 2019.
- [14] A. Simonelli, S. Rota Bulò, L. Porzi, M. Lopez-Antequera, and P. Kontschieder, "Disentangling monocular 3d object detection," in *ICCV*, 2019.
- [15] G. Brazil and X. Liu, "M3d-rpn: Monocular 3d region proposal network for object detection," in *arXiv preprint arXiv:1907.06038*, 2019.
- [16] T. Wang, X. Zhu, J. Pang, and D. Lin, "Fcos3d: Fully convolutional one-stage monocular 3d object detection," *arXiv preprint arXiv:2104.10956*, 2021.
- [17] Y. Wang, W.-L. Chao, D. Garg, B. Hariharan, M. Campbell, and K. Q. Weinberger, "Pseudo-lidar from visual depth estimation: Bridging the gap in 3d object detection for autonomous driving," in *CVPR*, 2019, pp. 8445–8453.
- [18] X. Ma, Z. Wang, H. Li, W. Ouyang, and P. Zhang, "Accurate monocular 3d object detection via color-embedded 3d reconstruction for autonomous driving," in *arXiv preprint arXiv:1903.11444*, 2019.
- [19] Y. You, Y. Wang, W.-L. Chao, D. Garg, G. Pleiss, B. Hariharan, M. Campbell, and K. Q. Weinberger, "Pseudo-lidar++: Accurate depth for 3d object detection in autonomous driving," in *ICLR*, 2020.
- [20] S. Shi, X. Wang, and H. Li, "Pointcnn: 3d object proposal generation and detection from point cloud," in *CVPR*, 2019, pp. 770–779.
- [21] Y. Yan, Y. Mao, and B. Li, "Second: Sparsely embedded convolutional detection," in *Sensors*, 2018.
- [22] Y. Zhou and O. Tuzel, "Voxelnet: End-to-end learning for point cloud based 3d object detection," in *CVPR*, 2018.
- [23] Y. Chen, S. Liu, X. Shen, and J. Jia, "Dsgn: Deep stereo geometry network for 3d object detection," in *CVPR*, 2020, pp. 12 536–12 545.
- [24] Y. Wang, B. Yang, R. Hu, M. Liang, and R. Urtasun, "Plume: Efficient 3d object detection from stereo images," in *2020 IEEE/RSJ International Conference on Intelligent Robots and Systems (IROS)*, 2021.
- [25] R. Qian, D. Garg, Y. Wang, Y. You, S. Belongie, B. Hariharan, M. Campbell, K. Q. Weinberger, and W.-L. Chao, "End-to-end pseudo-lidar for image-based 3d object detection," in *CVPR*, 2020, pp. 5881–5890.
- [26] C. Reading, A. Harakeh, J. Chae, and S. L. Waslander, "Categorical depth distribution network for monocular 3d object detection," *CVPR*, 2021.
- [27] X. Guo, S. Shi, X. Wang, and H. Li, "Liga-stereo: Learning lidar geometry aware representations for stereo-based 3d detector," in *ICCV*, 2021, pp. 3153–3163.
- [28] R. T. Collins, "A space-sweep approach to true multi-image matching," in *CVPR. IEEE*, 1996, pp. 358–363.
- [29] J. Flynn, I. Neulander, J. Philbin, and N. Snavely, "Deepstereo: Learning to predict new views from the world's imagery," in *CVPR*, 2016, pp. 5515–5524.
- [30] Y. Yao, Z. Luo, S. Li, T. Fang, and L. Quan, "Mvsnet: Depth inference for unstructured multi-view stereo," in *ECCV*, 2018, pp. 767–783.
- [31] G. Ghiasi, Y. Cui, A. Srinivas, R. Qian, T.-Y. Lin, E. D. Cubuk, Q. V. Le, and B. Zoph, "Simple copy-paste is a strong data augmentation method for instance segmentation," in *CVPR*, 2021, pp. 2918–2928.
- [32] A. Geiger, P. Lenz, and R. Urtasun, "Are we ready for autonomous driving? the kitti vision benchmark suite," in *CVPR*, 2012.
- [33] J. Ku, M. Mozifian, J. Lee, A. Harakeh, and S. Waslander, "Joint 3d proposal generation and object detection from view aggregation," in *IROS*, 2018.
- [34] F. Zhang, V. Prisacariu, R. Yang, and P. H. Torr, "Ga-net: Guided aggregation net for end-to-end stereo matching," in *CVPR*, 2019, pp. 185–194.
- [35] X. Guo, K. Yang, W. Yang, X. Wang, and H. Li, "Group-wise correlation stereo network," in *CVPR*, 2019.
- [36] D. Sun, X. Yang, M.-Y. Liu, and J. Kautz, "Pwc-net: Cnns for optical flow using pyramid, warping, and cost volume," in *CVPR*, 2018, pp. 8934–8943.
- [37] Y. Wang, Z. Lai, G. Huang, B. H. Wang, L. van der Maaten, M. Campbell, and K. Q. Weinberger, "Anytime stereo image depth estimation on mobile devices," in *ICRA. IEEE*, 2019, pp. 5893–5900.
- [38] N. Mayer, E. Ilg, P. Hausser, P. Fischer, D. Cremers, A. Dosovitskiy, and T. Brox, "A large dataset to train convolutional networks for disparity, optical flow, and scene flow estimation," in *CVPR*, 2016, pp. 4040–4048.
- [39] Z. Yin, T. Darrell, and F. Yu, "Hierarchical discrete distribution decomposition for match density estimation," in *CVPR*, 2019, pp. 6044–6053.
- [40] G. Yang, H. Zhao, J. Shi, Z. Deng, and J. Jia, "Segstereo: Exploiting semantic information for disparity estimation," in *ECCV*, 2018, pp. 636–651.
- [41] Z. Liang, Y. Feng, Y. Guo, H. Liu, W. Chen, L. Qiao, L. Zhou, and J. Zhang, "Learning for disparity estimation through feature constancy," in *CVPR*, 2018, pp. 2811–2820.
- [42] X. Song, X. Zhao, H. Hu, and L. Fang, "Edgestereo: A context integrated residual pyramid network for stereo matching," in *ACCV*, 2018.
- [43] A. Kar, C. Häne, and J. Malik, "Learning a multi-view stereo machine," in *Advances in neural information processing systems*, 2017, pp. 365–376.
- [44] Y. Yao, Z. Luo, S. Li, T. Shen, T. Fang, and L. Quan, "Recurrent mvsnet for high-resolution multi-view stereo depth inference," in *CVPR*, 2019.
- [45] R. Chen, S. Han, J. Xu, and H. Su, "Point-based multi-view stereo network," in *ICCV*, 2019.
- [46] M. Ji, J. Gall, H. Zheng, Y. Liu, and L. Fang, "Surfacenet: An end-to-end 3d neural network for multiview stereopsis," in *ICCV*, 2017, pp. 2307–2315.
- [47] P.-H. Huang, K. Matzen, J. Kopf, N. Ahuja, and J.-B. Huang, "Deepmvs: Learning multi-view stereopsis," in *CVPR*, 2018, pp. 2821–2830.
- [48] X. Gu, Z. Fan, S. Zhu, Z. Dai, F. Tan, and P. Tan, "Cascade cost volume for high-resolution multi-view stereo and stereo matching," in *CVPR*, 2020.
- [49] X. Chen, H. Ma, J. Wan, B. Li, and T. Xia, "Multi-view 3d object detection network for autonomous driving," in *CVPR*, 2017.
- [50] A. H. Lang, S. Vora, H. Caesar, L. Zhou, J. Yang, and O. Beijbom, "Pointpillars: Fast encoders for object detection from point clouds," in *arXiv:1812.05784*, 2018.
- [51] Y. Chen, S. Liu, X. Shen, and J. Jia, "Fast point r-cnn," in *ICCV*, 2019, pp. 9775–9784.
- [52] C. R. Qi, H. Su, K. Mo, and L. J. Guibas, "Pointnet: Deep learning on point sets for 3d classification and segmentation," in *CVPR*, 2017.

- [53] C. R. Qi, L. Yi, H. Su, and L. J. Guibas, "Pointnet++: Deep hierarchical feature learning on point sets in a metric space," in *NeurIPS*, 2017.
- [54] Z. Yang, Y. Sun, S. Liu, X. Shen, and J. Jia, "Std: Sparse-to-dense 3d object detector for point cloud," in *ICCV*, 2019.
- [55] D. Xu, D. Anguelov, and A. Jain, "Pointfusion: Deep sensor fusion for 3d bounding box estimation," in *CVPR*, 2018.
- [56] Y. Chen, L. Tai, K. Sun, and M. Li, "Monopair: Monocular 3d object detection using pairwise spatial relationships," in *CVPR*, 2020, pp. 12 093–12 102.
- [57] X. Shi, Q. Ye, X. Chen, C. Chen, Z. Chen, and T.-K. Kim, "Geometry-based distance decomposition for monocular 3d object detection," *arXiv preprint arXiv:2104.03775*, 2021.
- [58] X. Shi, Z. Chen, and T.-K. Kim, "Distance-normalized unified representation for monocular 3d object detection," in *European Conference on Computer Vision*. Springer, 2020, pp. 91–107.
- [59] X. Zhou, D. Wang, and P. Krähenbühl, "Objects as points," in *arXiv preprint arXiv:1904.07850*, 2019.
- [60] X. Ma, Y. Zhang, D. Xu, D. Zhou, S. Yi, H. Li, and W. Ouyang, "Delving into localization errors for monocular 3d object detection," in *CVPR*, 2021, pp. 4721–4730.
- [61] L. Wang, L. Du, X. Ye, Y. Fu, G. Guo, X. Xue, J. Feng, and L. Zhang, "Depth-conditioned dynamic message propagation for monocular 3d object detection," in *CVPR*, 2021, pp. 454–463.
- [62] X. Chen, K. Kundu, Y. Zhu, A. G. Berneshawi, H. Ma, S. Fidler, and R. Urtasun, "3d object proposals for accurate object class detection," in *NeurIPS*, 2015, pp. 424–432.
- [63] X. Chen, K. Kundu, Y. Zhu, H. Ma, S. Fidler, and R. Urtasun, "3d object proposals using stereo imagery for accurate object class detection," in *IEEE T-PAMI*. IEEE, 2017, pp. 1259–1272.
- [64] A. D. Pon, J. Ku, C. Li, and S. L. Waslander, "Object-centric stereo matching for 3d object detection," in *ICRA*. IEEE, 2020, pp. 8383–8389.
- [65] T. Roddick, A. Kendall, and R. Cipolla, "Orthographic feature transform for monocular 3d object detection," in *British Machine Vision Conference*, 2019.
- [66] J. Philion and S. Fidler, "Lift, splat, shoot: Encoding images from arbitrary camera rigs by implicitly unprojecting to 3d," in *ECCV*, 2020.
- [67] D. Garg, Y. Wang, B. Hariharan, M. Campbell, K. Weinberger, and W.-L. Chao, "Wasserstein distances for stereo disparity estimation," in *NeurIPS*, 2020.
- [68] S. Gupta, J. Hoffman, and J. Malik, "Cross modal distillation for supervision transfer," in *CVPR*, 2016, pp. 2827–2836.
- [69] P. Fischer, A. Dosovitskiy, E. Ilg, P. Häusser, C. Hazırbaş, V. Golkov, P. Van der Smagt, D. Cremers, and T. Brox, "Flownet: Learning optical flow with convolutional networks," *arXiv preprint arXiv:1504.06852*, 2015.
- [70] T. Zhou, R. Tucker, J. Flynn, G. Fyffe, and N. Snavely, "Stereo magnification: Learning view synthesis using multiplane images," *arXiv preprint arXiv:1805.09817*, 2018.
- [71] Y. Bengio and O. Delalleau, "On the expressive power of deep architectures," in *International conference on algorithmic learning theory*. Springer, 2011, pp. 18–36.
- [72] J. Kileel, M. Trager, and J. Bruna, "On the expressive power of deep polynomial neural networks," *Advances in Neural Information Processing Systems*, vol. 32, pp. 10 310–10 319, 2019.
- [73] A. Gupta, P. Dollar, and R. Girshick, "Lvis: A dataset for large vocabulary instance segmentation," in *CVPR*, 2019, pp. 5356–5364.
- [74] Z. Xu, W. Zhang, X. Ye, X. Tan, W. Yang, S. Wen, E. Ding, A. Meng, and L. Huang, "Zoomnet: Part-aware adaptive zooming neural network for 3d object detection," in *AAAI*, vol. 2, 2020, p. 7.
- [75] J. Sun, L. Chen, Y. Xie, S. Zhang, Q. Jiang, X. Zhou, and H. Bao, "Disp r-cnn: Stereo 3d object detection via shape prior guided instance disparity estimation," in *CVPR*, 2020, pp. 10 548–10 557.
- [76] C. Li, J. Ku, and S. L. Waslander, "Confidence guided stereo 3d object detection with split depth estimation," in *IROS*. IEEE, 2020, pp. 5776–5783.
- [77] Y. Liu, L. Wang, and M. Liu, "Yolostereo3d: A step back to 2d for efficient stereo 3d detection," in *ICRA*. IEEE, 2021.
- [78] D. P. Kingma and J. Ba, "Adam: A method for stochastic optimization," in *arXiv:1412.6980*, 2014.
- [79] O. D. Team, "Openpcdet: An open-source toolbox for 3d object detection from point clouds," <https://github.com/open-mmlab/OpenPCDet>, 2020.
- [80] S. Shi, C. Guo, L. Jiang, Z. Wang, J. Shi, X. Wang, and H. Li, "Pv-rnn: Point-voxel feature set abstraction for 3d object detection," in *CVPR*, 2020, pp. 10 529–10 538.